

# Himalayan valley-floor widths controlled by tectonically driven exhumation

Received: 14 September 2022

Accepted: 26 June 2023

Published online: 31 July 2023

 Check for updatesFiona J. Clubb<sup>1</sup>✉, Simon M. Mudd<sup>2</sup>, Taylor F. Schildgen<sup>3,4</sup>, Peter A. van der Beek<sup>4</sup>, Rahul Devrani<sup>5</sup> & Hugh D. Sinclair<sup>2</sup>

Himalayan rivers transport around a gigaton of sediment annually to ocean basins. Mountain valleys are an important component of this routing system: storage in these valleys acts to buffer climatic and tectonic signals recorded by downstream sedimentary systems. Despite a critical need to understand the spatial distribution, volume and longevity of these valley fills, controls on valley location and geometry are unknown, and estimates of sediment volumes are based on assumptions of valley-widening processes. Here we extract over 1.5 million valley-floor width measurements across the Himalaya to determine the dominant controls on valley-floor morphology and to assess sediment-storage processes. Using random forest regression, we show that channel steepness, a proxy for rock uplift, is a first-order control on valley-floor width. On the basis of a dataset of 1,148 exhumation rates, we find that valley-floor width decreases as exhumation rate increases. Our results suggest that valley-floor width is controlled by long-term tectonically driven exhumation rather than by water discharge or bedrock erodibility and that valley widening predominantly results from sediment deposition along low-gradient valley floors rather than lateral bedrock erosion.

Valleys in mountain systems act as transient sinks for sediments that journey from sources on mountain hillslopes to their final resting place in forelands or ocean basins. This storage can buffer, shred or destroy propagating sedimentary signals<sup>1–3</sup>. Therefore, understanding the spatial distribution, volumes and longevity of valley sediment fills is essential to reconstruct landscape evolution from sedimentary archives. However, controls on the spatial distribution of valley fills across the Himalaya are currently unknown. Past efforts to map the volumes and residence times of valley fills at scale<sup>4</sup> rely on the assumption that topography underneath the valley surface is similar to that of the exposed side slopes and therefore that little lateral erosion of the valley walls has taken place.

To explore valley widening, we consider a conceptual model where channels may either abrade or deposit sediment based on the ratio of sediment supply ( $Q_s$ ) to transport capacity ( $Q_c$ ) (Fig. 1). In channels with

low  $Q_s/Q_c$ , little sediment will be deposited on the valley floor, resulting in bedrock incision, whereas channels with high  $Q_s/Q_c$  will deposit thick valley fills with subsequent valley widening<sup>5–9</sup>.

We can consider low  $Q_s/Q_c$  channels to behave similarly to the detachment-limited model for vertical incision, commonly used in mountain landscapes (for example, ref. 10). In this case, valley-floor width changes occur through lateral erosion of the valley walls and the balance between vertical incision and lateral erosion. Wall erosion is likely to occur when the channel is frequently in contact with the walls<sup>6,11</sup>, such as in narrow valleys. Valley-floor width  $W_v$  in this case has been suggested to scale with bank-full water discharge  $Q_w$ , modulated by an erodibility coefficient  $K$  reflecting the impact of lithology (for example, refs. 12–16):

$$W_v = KQ_w^c \quad (1)$$

<sup>1</sup>Department of Geography, Durham University, Durham, UK. <sup>2</sup>School of GeoSciences, University of Edinburgh, Edinburgh, UK. <sup>3</sup>GFZ German Research Centre for Geosciences, Potsdam, Germany. <sup>4</sup>Institute for Geosciences, University of Potsdam, Potsdam, Germany. <sup>5</sup>Jindal School of Environment and Sustainability, OP Jindal Global University, Sonapat, India. ✉e-mail: [fiona.j.clubb@durham.ac.uk](mailto:fiona.j.clubb@durham.ac.uk)

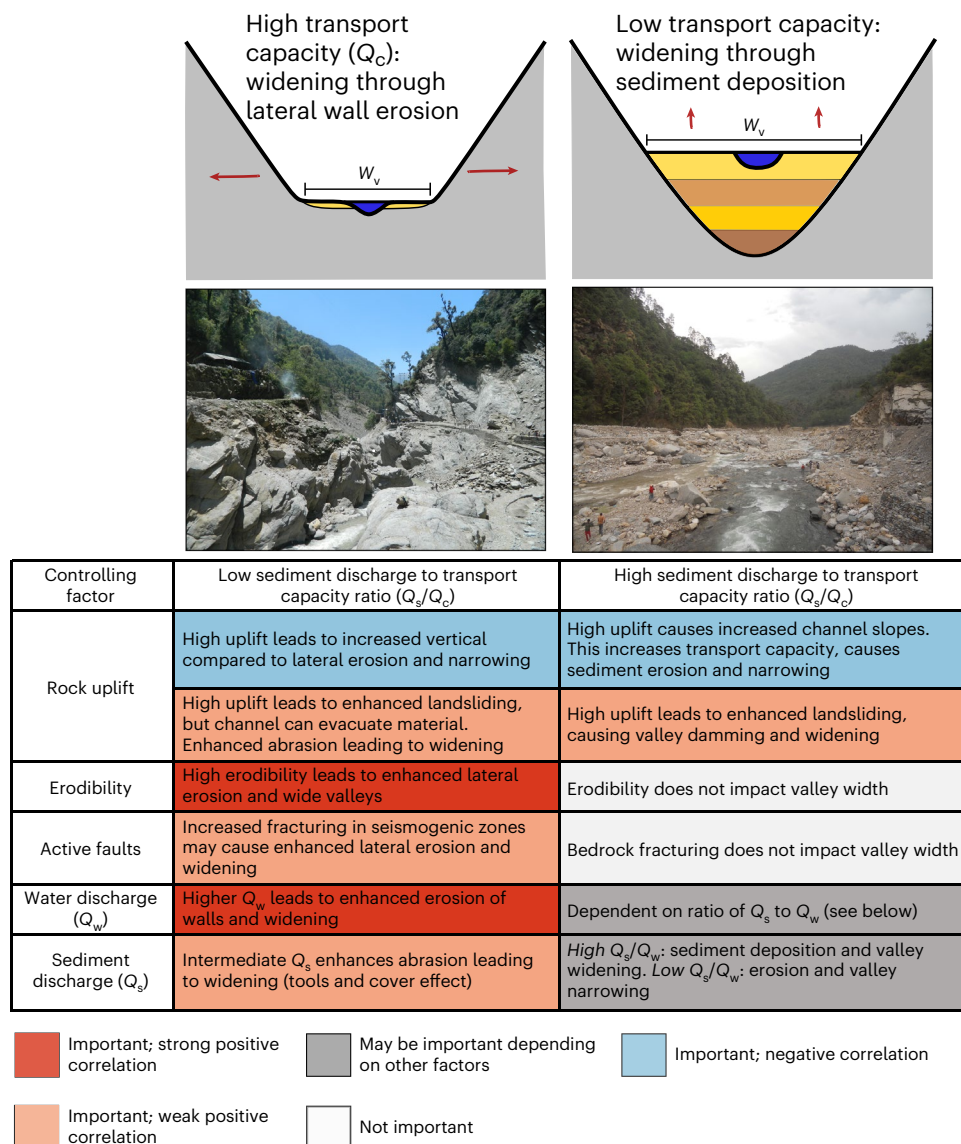


**Fig. 1** End members of sediment-transport capacity model of valley-widening mechanisms and different factors that may control valley-width changes in each scenario. The photographs show examples of the two end-

member valley types in the Upper Ganga basin (photo credit: R. Devrani).  $W_v$ , valley-floor width;  $Q_w$ , water discharge;  $Q_s$ , sediment supply.

In landscapes transiently adjusting to changes in rock-uplift rate, this relationship has been shown to break down (for example, refs. 17,18). An alternative formulation postulates that valley width is also dependent on valley slope ( $S$ )<sup>11,17</sup> (Supplementary equations (1)–(5)).

Despite its common application, this low  $Q_s/Q_c$  case is contradicted by field observations, which show that mountain valleys are often infilled with sediment (Fig. 1). In valleys with a high  $Q_s/Q_c$ , widening through wall erosion will only occur if lateral erosion rates greatly exceed vertical incision, such that the channel regularly moves across the valley floor, impinging upon sidewalls<sup>6,11</sup>. However,  $W_v$  can also change purely through sediment deposition and/or erosion, without lateral wall erosion. If we imagine a roughly V-shaped valley infilled with sediment (Fig. 1), then increasing sediment fill would widen the valley, whereas incision into the fill would narrow it.

These end members of  $Q_s/Q_c$  represent contrasting mechanisms of valley-floor width changes, which are controlled by different factors (Fig. 1). In both cases, rock uplift is likely to be an important control on  $W_v$ , because high uplift rates elevate channel slopes, decreasing  $Q_s/Q_c$  through increased flow velocity, resulting in narrowing and bedrock

incision<sup>17</sup>. Alternatively, increased frequency of landsliding in regions of high uplift (for example, ref. 19) could block channels, inducing upstream alluviation and widening.

The lithology of bedrock walls,  $K$ , is likely to be a more important control on  $W_v$ <sup>12,16</sup> in the low  $Q_s/Q_c$  end member. In a valley that changes width primarily due to sediment erosion or deposition, variations in  $K$  are unlikely to play a dominant role, as width is not set by lateral bedrock erosion. In the high  $Q_s/Q_c$  end member,  $K$  may influence sediment delivery to the channel and thus  $W_v$  by changing the size and resistance of sediment from hillslope failures or upstream sediment transport<sup>20</sup>. However, the complex interplay of upstream and lateral sediment supply and downstream sediment transport means that it would be challenging to link variations in sediment erodibility to  $W_v$  at each point along the channel. Faulting may also increase rock fracturing and therefore erodibility (for example, ref. 21): we might therefore expect that valleys in fractured zones (such as near seismogenic faults) would be wider where lateral erosion is important, but not in the high  $Q_s/Q_c$  model.

Equation (1) suggests that water discharge is an important control on  $W_v$ ; however, in our conceptual model, the ratio of sediment flux to

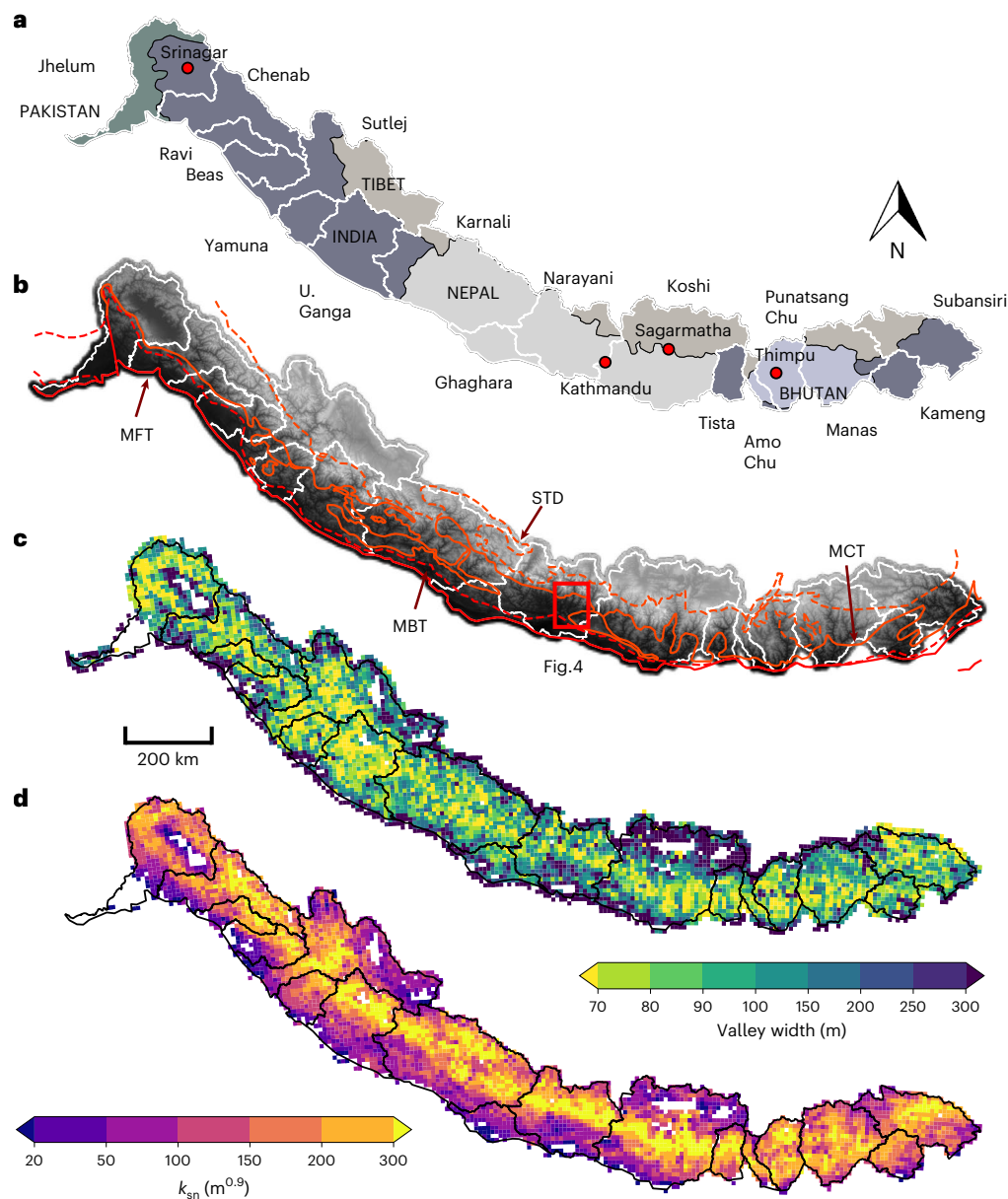


**Fig. 2 | Spatial distribution of valley-floor width and channel steepness across the Himalaya. a**, Map of the Himalayan orogen showing basins used for width analysis<sup>47</sup>. **b**, Topography across the region with main structural boundaries:

MFT, MBT, MCT, and STD. **c,d**, distribution of valley-floor width (**c**) and distribution of normalized channel steepness ( $k_{sn}$ ) across the Himalaya (**d**). The data in **c** and **d** are gridded into cells with 10 km spatial resolution.

water discharge,  $Q_s/Q_w$ , rather than  $Q_w$  alone, is likely to influence  $W_v$ . Field studies<sup>22,23</sup> and physical experiments<sup>7</sup> have demonstrated that a decrease in  $Q_s/Q_w$  leads to incision and valley narrowing, whereas an increase in  $Q_s/Q_w$  leads to sediment deposition and widening. Over orogenic scales, we therefore hypothesize that the correlation between  $W_v$  and  $Q_w$  would be complicated by spatial variations in sediment flux. Sediment-storage volume estimates across the Himalaya<sup>4</sup> implicitly use the high  $Q_s/Q_w$  end member because they assume that little erosion of the valley walls occurs to modify the valley-floor topography.

In this contribution, we investigate dominant controls on  $W_v$  across the Himalaya and test these end-member models of valley widening and sediment storage. We generate a dataset of valley-floor widths across the Himalaya and investigate the relative importance of hypothesized controls on  $W_v$  through random forest regression. We also explore links between  $W_v$ , channel steepness ( $k_{sn}$ ) and exhumation rate using a compilation of thermochronometric cooling ages<sup>24</sup>.

We use an automated method<sup>25,26</sup> to extract  $W_v$  from every major river basin in the Himalaya, resulting in 1,644,215 width measurements. We grid  $W_v$  into 10 km pixels to better reveal spatial trends: Fig. 2 shows the distribution of  $W_v$  across the orogen. We quantify each controlling factor that may affect  $W_v$  outlined in Fig. 1 (Methods).

### Controls on valley-floor width

Figure 3a shows a bimodal distribution of  $W_v$  with elevation, where valleys are widest at elevations  $<1,000$  m and  $>4,000$  m. We would expect the southern, low-elevation region to have wider valleys as discharge increases towards the foreland. Although we remove areas affected by glaciation (Methods), widening at high elevations also results from past glaciations. We tested for this by removing valleys affected by Last Glacial Maximum glaciation, but this did not alter the results (Supplementary Figs. 1 and 2). High elevations also correlate with lower  $k_{sn}$  (Extended Data Fig. 1) and erodible lithologies of the Tethyan Himalayan

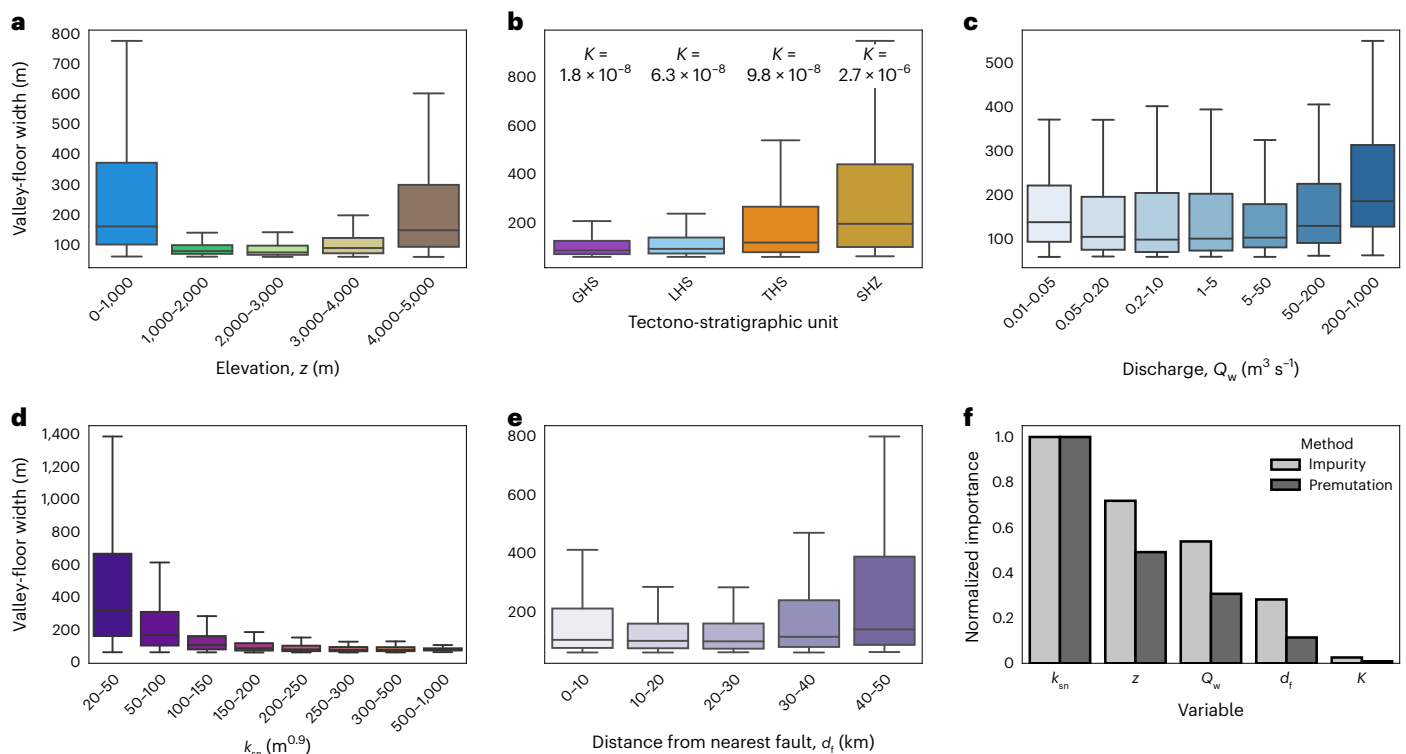


**Fig. 3 | Box plots of valley-floor width ( $n = 7,414$ ) against controlling variables. a**, Elevation,  $z$ . **b**, Tectono-stratigraphic unit, where erodibility values ( $K$ ,  $\text{m}^{1-2\text{m}} \text{yr}^{-1}$ ) for each unit are labelled. GHS = Greater Himalayan Sequence; SHZ = Sub Himalayan Zone. **c**, Water discharge,  $Q_w$  ( $\text{m}^3 \text{s}^{-1}$ ). **d**, **e**, Normalized channel steepness,  $k_{\text{sn}}$  ( $\text{m}^{0.9}$ ) (**d**) and distance from nearest major fault,  $d_f$  (km, MFT, MBT, MCT, or STD) (**e**). The solid black line shows the median of each distribution; the box represents the inter-quartile range; and the whiskers

represent 1.5 times the inter-quartile range. Minima and maxima have been omitted to ensure readability. **f**, The normalized importance of each variable using random forest regression with two different methods for calculating importance: weighted impurity reduction (light grey) and permutation reduction (dark grey). Normalization is performed by dividing each variable importance by the most important variable ( $k_{\text{sn}}$  in both cases).

Sequence (THS), suggesting that increased  $W_v$  at high elevations may be explained by other co-varying factors.

Figure 3b also shows that there is variation in median  $W_v$  among the main tectono-stratigraphic units. This is possibly due to lithological control on  $W_v$ , as the narrowest valleys are found in the high-grade gneisses and granites of the Greater Himalayan Sequence (GHS). The widest valleys are found in the sedimentary units of the Siwaliks in the Sub-Himalayan Zone (SHZ). However, these variations with tectono-stratigraphy co-correlate with elevation as discussed above, making it difficult to separate these two factors. Figure 3e shows there is little variation in  $W_v$  with distance from the major tectonic structures (MFT, MBT, MCT or STD), suggesting that increased erodibility through fracturing<sup>21</sup> is not enhancing wall erosion.

Rock-uplift rates across the Himalaya since the middle Miocene have been controlled primarily by the geometry of the Main Himalayan Thrust (MHT)<sup>27</sup>, a northward-dipping décollement, which is the basal detachment for the MFT, MBT and MCT. The MHT is thought to be relatively flat under much of the Lesser Himalayan Sequence (LHS), steeper to the north over a mid-crustal ramp (for example, ref. 28) beneath the GHS, then flat again beneath the THS (Fig. 4). The ramp is associated with faster rock-uplift rates and steeper topography<sup>29</sup>, with a ‘physiographic transition’ (PT) marking the change from the southern (shallower) flat to the ramp. In central Nepal, we find a distinct area of wide valley floors within the LHS, with the transition to narrow valleys north of the PT coinciding with increased exhumation rate (Fig. 4). Considering that the PT cuts across the LHS in this region, the flat-ramp-flat structure of the MHT appears to influence  $W_v$  in central Nepal more strongly than the transitions across tectono-stratigraphic units.

Existing valley-widening models predict a monotonic relationship between  $Q_w$  and  $W_v$  (equation (1)). Our results do not show this relationship (Fig. 3c). Although the widest valleys ( $99 \pm 280$  m) tend to coincide with intermediate  $Q_w$  of  $0.2\text{--}1.0 \text{ m}^3 \text{ yr}^{-1}$ . At the lowest  $Q_w$  of  $0.01\text{--}0.05 \text{ m}^3 \text{ yr}^{-1}$ , median  $W_v$  increases to  $139 \pm 169$  m. This lack of correlation suggests that in contrast to the commonly applied model of width evolution through lateral bedrock erosion,  $Q_w$  is not the dominant control on  $W_v$  across the actively uplifting Himalayan orogen.

There is, however, a negative correlation between  $W_v$  and  $k_{\text{sn}}$  (Fig. 3d). We tested this relationship across different tectono-stratigraphies and found it is consistent between lithologies (Extended Data Fig. 2). To account for the competing influence of  $Q_w$  and  $S$ , we also calculated a discharge-weighted channel steepness,  $k_{\text{sn-q}}$ <sup>30</sup>. We found this did not alter the relationship between  $k_{\text{sn}}$  and  $W_v$  (Supplementary Fig. 3).  $k_{\text{sn}}$  is a widely accepted proxy for rock-uplift rate (for example, ref. 31), suggesting that  $W_v$  responds to spatial variations in rock-uplift rate. We also find no relationship between  $W_v$  and mean annual rainfall (Extended Data Fig. 3).

To further test tectonic control of  $W_v$ , we use a compilation of 1,148 thermochronometric ages<sup>24</sup> (Fig. 5), from which we estimate exhumation rates ( $E$ ) using a simple 1D thermal model (Methods). Figure 5b,c shows a correlation between  $W_v$ ,  $E$  and  $k_{\text{sn}}$ . The lowest  $E$  of  $0.1\text{--}0.2 \text{ mm yr}^{-1}$  corresponds to the widest valleys and lowest  $k_{\text{sn}}$ . Intermediate  $E$  between  $0.3$  and  $0.9 \text{ mm yr}^{-1}$  show less variation in both  $W_v$  and  $k_{\text{sn}}$ , whereas  $E \geq 2 \text{ mm yr}^{-1}$  correspond to narrow valley floors and steep channels. Variations in  $E$  in the Himalaya have been argued to be strongly tectonically controlled<sup>27,32,33</sup>. The correlation between  $W_v$  and  $E$ , along with the changes in  $W_v$  across the flat-ramp-flat

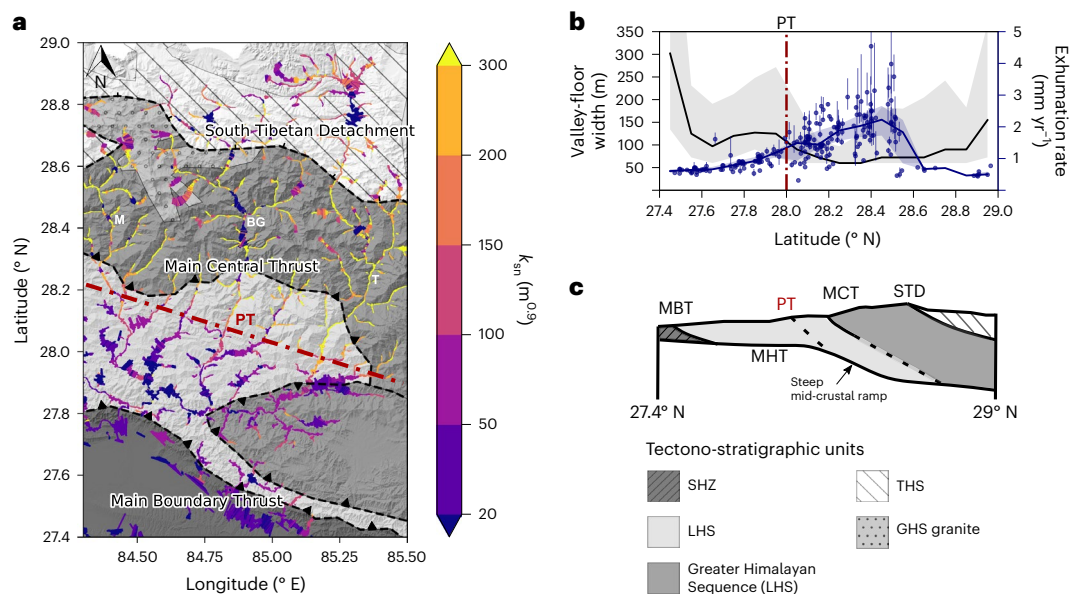


**Fig. 4 | The impact of tectonics on valley-floor widths.** **a**, Illustration of valley-floor width across part of the Narayani basin in central Nepal, where line width is scaled by valley-floor width (widths are scaled up for visibility), and line colour represents channel steepness ( $k_{sn}$ ). The dashed lines show the main structural boundaries. Note the presence of glacially widened valleys in the Greater Himalayan Sequence, and the distinct valley widening and flattening to the south of the physiographic transition (PT) within the LHS. M, Marsyandi river; BG, Budhi Gandaki River; T, Trishuli river. **b**, Median valley-floor width (black

line,  $n = 81,208$ ) and exhumation rate derived from thermochronometry<sup>24</sup> (blue line,  $n = 218$ ) binned by 0.1° latitude across the region shown in **a**, showing valley narrowing and rapid exhumation to the north of the PT at the location of the MHT mid-crustal ramp. The shaded areas show the range between the 25th and 75th percentiles. The points show the exhumation rate samples where the error bars represent the  $1\sigma$  uncertainty in exhumation rate. **c**, Schematic cross-section across the region in **a** showing the location of the mid-crustal ramp within the MHT (modified from ref. 48).

geometry of the MHT (Fig. 4), indicate that  $W_v$  is probably controlled by tectonics.

Thermochronologic cooling ages are representative of exhumation over long timescales ( $10^5$  to  $10^7$  years)<sup>34</sup>. Patterns of exhumation across the Himalaya are likely to change through time with tectonic or climatic variations (for example, refs. 35–37), potentially disconnecting long-term exhumation measurements and valley-forming processes. We focus here on thermochronometry rather than cosmogenic radionuclide-derived (CRN) erosion rates because the spatial coverage of thermochronometric data is far greater than CRN and because the relationship between  $W_v$  and  $A$  makes it challenging to determine a representative  $W_v$  to compare with catchment-averaged erosion rates. Examining  $W_v$  and  $E$  separately by thermochronometer (Extended Data Fig. 4) shows that the relationship between  $W_v$  and  $E$  is strongest in chronometers with lower closure temperatures, representing more recent exhumation rates. Nevertheless, the correlations between  $W_v$ ,  $k_{sn}$  and  $E$  across the dataset (Fig. 5) indicate a tectonic control on  $W_v$  and  $k_{sn}$  despite potential temporal variations.

### Importance of valley-floor width controls

Figure 3a–e demonstrates that many factors may control  $W_v$  across the Himalayan orogen; we therefore take a data-driven approach to determine which has the strongest influence using random forest (RF) regression. To explore key controls on  $W_v$ , we focus on the following variables based on our conceptual model (Fig. 1): (1) elevation,  $z$ ; (2)  $k_{sn}$ ; (3)  $Q_w$ ; (4)  $K$ ; and (5) distance from the nearest fault,  $d_f$  (MFT, MBT, MCT or STD). We calculate  $K$  using CRN-derived erosion rates and  $k_{sn}$  (Methods).

RF-regression estimates of variable importance (Methods) indicate that  $k_{sn}$  is the most important predictor across all regression models (Fig. 3f), with  $K$  consistently the least important.  $z$ ,  $Q_w$  and  $d_f$  have relatively similar importance, although  $z$  tends to be more important among these three. There are distinct spatial trends in  $k_{sn}$  with  $z$ , with

highest  $k_{sn}$  found at intermediate  $z$  and lower  $k_{sn}$  at both low and high  $z$  (Extended Data Fig. 1). This co-variation may explain the high relative importance of  $z$  in the RF model.

### Implications for valley-widening processes

Our results indicate moderate importance of  $Q_w$  and low importance of  $K$  on  $W_v$ , contrasting with common valley-widening models (equation (1)). We propose that observed  $W_v$  are likely set by sediment accumulation, corresponding to the higher  $Q_s/Q_c$  end member in Fig. 1. This suggests little modification of topography under these fills, supporting a key assumption of Himalayan sediment volume estimates<sup>4</sup>. For a given  $Q_s$  and  $Q_w$ , the likelihood of a channel to incise or aggrade is set by  $S$ , dependent on uplift. The relationship between  $E$ ,  $k_{sn}$  and  $W_v$  indicates that high rock-uplift rates in rapidly exhuming regions, reflected by high values of  $k_{sn}$ , are likely to increase  $Q_c$ , mobilizing sediment that acts as tools for bedrock incision during peak  $Q_w$ , with subsequent valley-floor narrowing. Therefore, rivers in high-uplift regions are likely to typify the low  $Q_s/Q_c$  end member, whereas slowly uplifting regions exemplify the higher  $Q_s/Q_c$  scenario. Nevertheless, the low importance of  $K$  suggests that sediment is important across the full range of  $E$  and that even under the highest rock-uplift rates, rivers are likely to contain substantial alluvial cover, with bedrock incision only during extreme transport events.

Damming behind landslides or uplifting structures increases  $W_v$  upstream. Considering that landslides occur more frequently in rapid exhumation regions<sup>19</sup>, a landslide-dam control on  $W_v$  at the orogen scale would generate wider valley floors in faster exhuming regions (Fig. 1), or at least highly variable widths. In contrast, if damming behind uplifting structures (for example, refs. 38,39) controlled  $W_v$ , wider valleys may be randomly distributed. We find that  $k_{sn}$  is a first-order control on  $W_v$  and that  $k_{sn}$  increases and  $W_v$  decreases with  $E$ . This implies that the distribution of valley fills is driven by tectonically controlled exhumation, rather than landsliding or structural damming. An exception is that at

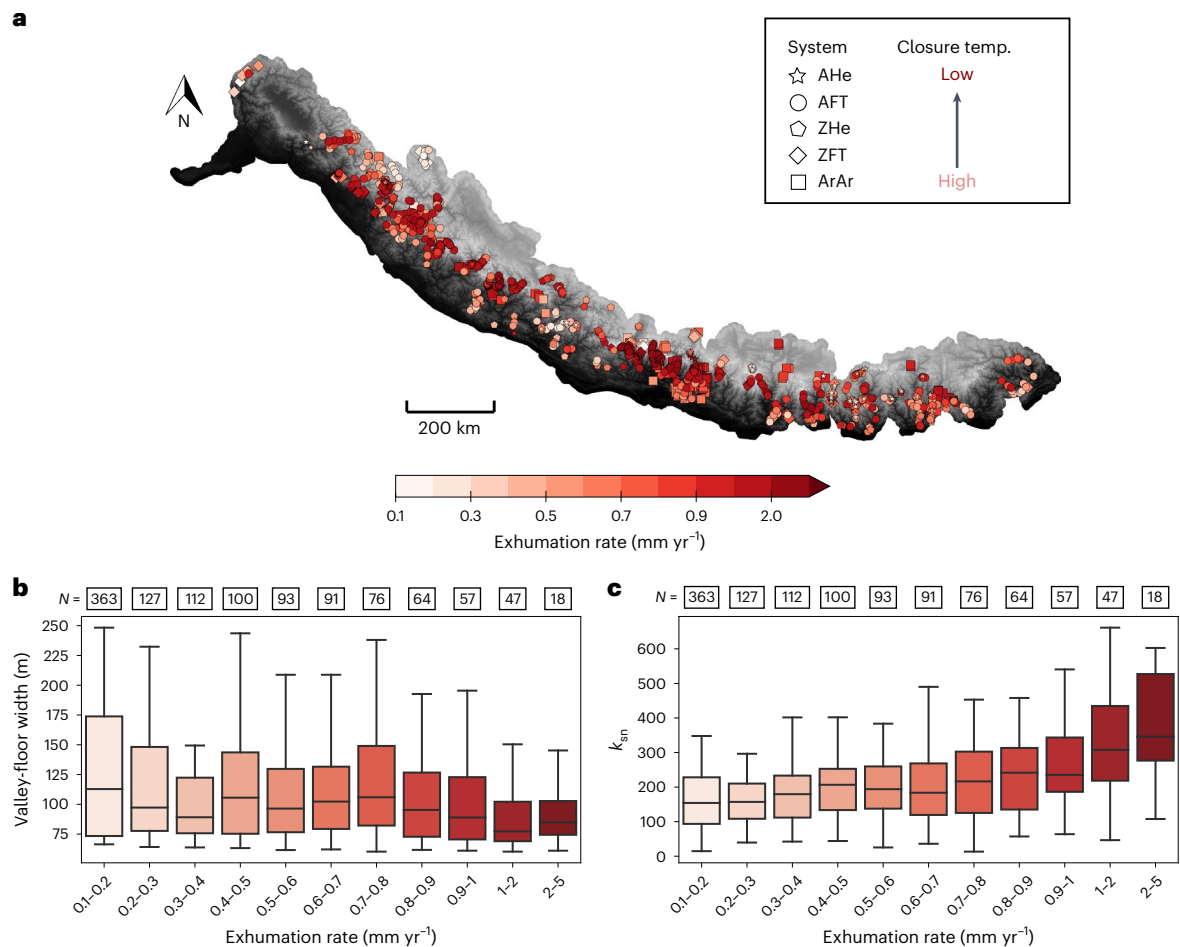


**Fig. 5 | The relationship between valley-floor width, channel steepness and exhumation rate.** **a**, Map of exhumation rate derived from thermochronometry data across the Himalaya: the colours represent the exhumation rate in  $\text{mm yr}^{-1}$ , symbols represent the thermochronometric system. AHe: apatite (U-Th)/He; AFT: apatite fission track; ZHe: zircon (U-Th)/He; ZFT: zircon fission track; ArAr:  $^{40}\text{Ar}/^{39}\text{Ar}$ . **b**, Box plots showing relationship between valley-floor width and

exhumation rate: the numbers above each box show the number of samples in the corresponding bin ( $n = 1,148$ ). **c**, Box plots showing the relationship between normalized channel steepness ( $k_{sn}$ ) and exhumation rate ( $n = 1,148$ ). The solid black line shows the median of each distribution; the box represents the inter-quartile range; and the whiskers represent 1.5 times the inter-quartile range. Minima and maxima have been omitted to ensure readability.

intermediate  $E$  of  $0.3\text{--}0.9 \text{ mm yr}^{-1}$ , increased  $E$  does not lead to concomitant changes in  $k_{sn}$  or  $W_v$ . If at these intermediate exhumation rates, channels are insufficiently steep to regularly flush aggraded sediment, the impact of landslide and structural damming could be enhanced.

Although our results point to  $W_v$  being set by the depth of sediment fill rather than wall erosion, valleys must experience lateral erosion during their evolutionary history. The  $Q_s/Q_c$  ratio may vary during climate oscillations<sup>5,6</sup>, leading to alternating periods of bedrock incision and widening through wall erosion and periods of sediment deposition and filling. However, valleys that are currently alluviated must also facilitate bedrock erosion to adjust to long-term uplift rates. The frequency of incision should be limited to the most extreme events that can remobilize valley fills<sup>40–43</sup>. Recent work shows that valleys regularly affected by glacial lake outburst floods (GLOFs) are generally narrower and contain less sediment, facilitating bedrock erosion, while valleys with less frequent GLOFs showed sediment trapping and lower incision rates<sup>44</sup>. Along the Bhote Koshi River, GLOFs were observed to mobilize the largest boulders<sup>41</sup>, indicating that they can effectively flush valleys and cause bedrock erosion.

Our findings raise questions about the residence times of valley-fill deposits compared to extreme event frequencies. The adjustment of  $W_v$  to  $E$  averaged over  $10^5\text{--}10^7$ -year timescales indicates either that valley fills persist over geological timescales or that  $W_v$  adjusts relatively rapidly to the local exhumation rate. Residence times of Himalayan

fills have been proposed to exceed  $10^5$  years for the largest valleys<sup>4</sup>. Recurrence intervals of extreme events are likely shorter, with the Bhote Koshi River affected by GLOFs with a return interval of  $\approx 30$  years<sup>45</sup>, although it is unlikely that every GLOF will strip all sediment from the valley floor. Dating of far-travelled boulders in the Trishuli and Sunkoshi rivers indicated a recurrence interval of  $\approx 5$  thousand years for the most extreme GLOFs<sup>46</sup>. Our results suggest that valley re-filling to adjust to local exhumation occurs on shorter timescales than valley-fill removal.

The link between  $E$  and  $W_v$  also has important implications for sediment routing systems and the transmission of sedimentary signals to basins. If slower exhumation rates lead to wider valleys, then sedimentary signals of external forcing in slowly exhuming areas are likely to spend more time in storage compared to rapidly exhuming areas, resulting in either buffering or shredding of the signal before it reaches its depositional sink (for example, refs. 2,3). Future work is needed to further explore (1) the timescales of Himalayan valley-fill preservation; (2) the impact of exhumation rate on the propagation of allogenic signals and (3) the sub-surface geometry of valley deposits to allow further investigation into valley-widening mechanisms.

### Online content

Any methods, additional references, Nature Portfolio reporting summaries, source data, extended data, supplementary information,

acknowledgements, peer review information; details of author contributions and competing interests; and statements of data and code availability are available at <https://doi.org/10.1038/s41561-023-01238-8>.

## References

- Castelltort, S. & Van Den Driessche, J. How plausible are high-frequency sediment supply-driven cycles in the stratigraphic record? *Sediment. Geol.* **157**, 3–13 (2003).
- Jerolmack, D. J. & Paola, C. Shredding of environmental signals by sediment transport. *Geophys. Res. Lett.* **37**, L19401 (2010).
- Straub, K. M. et al. Buffered, incomplete, and shredded: the challenges of reading an imperfect stratigraphic record. *J. Geophys. Res. Earth Surf.* **125**, e2019JF005079 (2020).
- Blöthe, J. H. & Korup, O. Millennial lag times in the Himalayan sediment routing system. *Earth Planet. Sci. Lett.* **382**, 38–46 (2013).
- Bull, W. B. Stream-terrace genesis: implications for soil development. *Geomorphology* **3**, 351–367 (1990).
- Hancock, G. S. & Anderson, R. S. Numerical modeling of fluvial strath-terrace formation in response to oscillating climate. *Geol. Soc. Am. Bull.* **11**, 1131–1142 (2002).
- Tofelde, S., Savi, S., Wickert, A. D., Bufe, A. & Schildgen, T. F. Alluvial channel response to environmental perturbations: fill-terrace formation and sediment-signal disruption. *Earth Surf. Dyn.* **7**, 609–631 (2019).
- Baynes, E. R., Lague, D. & Kermarrec, J. J. Supercritical river terraces generated by hydraulic and geomorphic interactions. *Geology* **46**, 499–502 (2018).
- Bufe, A. et al. Controls on the lateral channel-migration rate of braided channel systems in coarse non-cohesive sediment. *Earth Surf. Process. Landforms* **44**, 2823–2836 (2019).
- Whipple, K. X. Bedrock rivers and the geomorphology of active orogens. *Annu. Rev. Earth Planet. Sci.* **32**, 151–185 (2004).
- Brocard, G. & van der Beek, P. Influence of incision rate, rock strength, and bedload supply on bedrock river gradients and valley-flat widths: field-based evidence and calibrations from western Alpine rivers (southeast France). *Geol. Soc. Am. Spec. Pap.* **398**, 101–126 (2006).
- Tomkin, J. H., Brandon, M. T., Pazzaglia, F. J., Barbour, J. R. & Willett, S. D. Quantitative testing of bedrock incision models for the Clearwater River, NW Washington State. *J. Geophys. Res.* **108**, 2308 (2003).
- Snyder, N. P., Whipple, K. X., Tucker, G. E. & Merritts, D. J. Channel response to tectonic forcing: field analysis of stream morphology and hydrology in the Mendocino triple junction region, northern California. *Geomorphology* **53**, 97–127 (2003).
- May, C., Roering, J., Eaton, L. & Burnett, K. Controls on valley width in mountainous landscapes: the role of landsliding and implications for salmonid habitat. *Geology* **41**, 503–506 (2013).
- Beeson, H. W., Flitcroft, R. L., Fonstad, M. A. & Roering, J. J. Deep-seated landslides drive variability in valley width and increase connectivity of salmon habitat in the Oregon Coast Range. *JAWRA J. Am. Water Resour. Assoc.* **54**, 1325–1340 (2018).
- Langston, A. L. & Temme, A. J. A. M. Impacts of lithologically controlled mechanisms on downstream bedrock valley widening. *Geophys. Res. Lett.* **46**, 12056–12064 (2019).
- Finnegan, N. J., Roe, G., Montgomery, D. R. & Hallet, B. Controls on the channel width of rivers: implications for modeling fluvial incision of bedrock. *Geology* **33**, 229–232 (2005).
- Whittaker, A. C., Cowie, P. A., Attal, M., Tucker, G. E. & Roberts, G. P. Bedrock channel adjustment to tectonic forcing: implications for predicting river incision rates. *Geology* **35**, 103–106 (2007).
- Larsen, I. J. & Montgomery, D. R. Landslide erosion coupled to tectonics and river incision. *Nat. Geoscience* **5**, 468–473 (2012).
- Shobe, C. M. et al. The role of infrequently mobile boulders in modulating landscape evolution and geomorphic hazards. *Earth Sci. Rev.* **220**, 103717 (2021).
- Kirkpatrick, H. M., Moon, S., Yin, A. & Harrison, T. M. Impact of fault damage on eastern Tibet topography. *Geology* **49**, 30–34 (2021).
- Miller, D. J. & Benda, L. E. Effects of punctuated sediment supply on valley-floor landforms and sediment transport. *Geol. Soc. Am. Bull.* **13**, 1814–1824 (2000).
- Schildgen, T. et al. Landscape response to late Pleistocene climate change in NW Argentina: sediment flux modulated by basin geometry and connectivity. *J. Geophys. Res. Earth Surf.* **121**, 392–414 (2016).
- van der Beek, P. & Schildgen, T. F. Short communication: age2exhume—a MATLAB/Python script to calculate steady-state vertical exhumation rates from thermochronometric ages and application to the Himalaya. *Geochronology* **5**, 35–49 (2023).
- Clubb, F. et al. Geomorphometric delineation of floodplains and terraces from objectively defined topographic thresholds. *Earth Surf. Dyn.* **5**, 369–385 (2017).
- Clubb, F. J., Weir, E. F. & Mudd, S. M. Continuous measurements of valley floor width in mountainous landscapes. *Earth Surf. Dyn.* **10**, 437–456 (2022).
- Zilio, L. D., Hetényi, G., Hubbard, J. & Bollinger, L. Building the Himalaya from tectonic to earthquake scales. *Nat. Rev. Earth Environ.* **2**, 251–268 (2021).
- Nábělek, J. et al. Underplating in the Himalaya–Tibet collision zone revealed by the Hi-CLIMB experiment. *Science* **325**, 1371–1374 (2009).
- Hodges, K. V., Hurtado, J. M. & Whipple, K. X. Southward extrusion of Tibetan crust and its effect on Himalayan tectonics. *Tectonics* **20**, 799–809 (2001).
- Adams, B. A., Whipple, K. X., Forte, A. M., Heimsath, A. M. & Hodges, K. V. Climate controls on erosion in tectonically active landscapes. *Sci. Adv.* **6**, 3166–3182 (2020).
- Scherler, D., Bookhagen, B. & Strecker, M. R. Tectonic control on <sup>10</sup>Be-derived erosion rates in the Garhwal Himalaya, India. *J. Geophys. Res. Earth Surf.* **119**, 83–105 (2014).
- Robert, X., van der Beek, P., Braun, J., Perry, C. & Mugnier, J. L. Control of detachment geometry on lateral variations in exhumation rates in the Himalaya: insights from low-temperature thermochronology and numerical modeling. *J. Geophys. Res.* **116**, 5202 (2011).
- van der Beek, P. et al. Contrasting tectonically driven exhumation and incision patterns, western versus central Nepal Himalaya. *Geology* **44**, 327–330 (2016).
- Reiners, P. W. & Brandon, M. T. Using thermochronology to understand orogenic erosion. *Annu. Rev. Earth Planet. Sci.* **34**, 419–466 (2006).
- Grujic, D. et al. Climatic forcing of erosion, landscape, and tectonics in the Bhutan Himalayas. *Geology* **34**, 801–804 (2006).
- Clift, P. D. et al. Correlation of Himalayan exhumation rates and Asian monsoon intensity. *Nat. Geoscience* **1**, 875–880 (2008).
- Herman, F. et al. Exhumation, crustal deformation, and thermal structure of the Nepal Himalaya derived from the inversion of thermochronological and thermobarometric data and modeling of the topography. *J. Geophys. Res.* **115**, 6407 (2010).
- Wang, P. et al. Tectonic control of Yarlung Tsangpo Gorge revealed by a buried canyon in Southern Tibet. *Science* **346**, 978–981 (2014).
- Adams, B. A. et al. In situ development of high-elevation, low-relief landscapes via duplex deformation in the Eastern Himalayan hinterland, Bhutan. *J. Geophys. Res. Earth Surf.* **121**, 294–319 (2016).
- Devrani, R., Singh, V., Mudd, S. M. & Sinclair, H. D. Prediction of flash flood hazard impact from Himalayan river profiles. *Geophys. Res. Lett.* **42**, 5888–5894 (2015).

41. Cook, K. L., Andermann, C., Gimbert, F., Adhikari, B. R. & Hovius, N. Glacial lake outburst floods as drivers of fluvial erosion in the Himalaya. *Science* **362**, 53–57 (2018).
42. Panda, S. et al. Chronology and sediment provenance of extreme floods of Siang River (Tsangpo-Brahmaputra River valley), northeast Himalaya. *Earth Surf. Process. Landforms* **45**, 2495–2511 (2020).
43. Graf, E. L. et al. Geomorphological and hydrological controls on sediment export in earthquake-affected catchments in the Nepal Himalaya. Preprint at *EGUsphere* <https://doi.org/10.5194/egusphere-2022-1347> (2023).
44. Dahlquist, M. P. & West, A. J. The imprint of erosion by glacial lake outburst floods in the topography of central Himalayan rivers. *Earth Surf. Dyn.* **10**, 705–722 (2022).
45. Mool, P. K. Glacier lake outburst floods in Nepal. *J. Nepal Geol. Soc.* **11**, 273–280 (1995).
46. Huber, M. L., Lupker, M., Gallen, S. F., Christl, M. & Gajurel, A. P. Timing of exotic, far-traveled boulder emplacement and paleo-outburst flooding in the central Himalayas. *Earth Surf. Dyn.* **8**, 769–787 (2020).
47. Sub-basins of Hindu Kush Himalaya (HKH) Region ICIMOD <https://doi.org/10.26066/RDS.8909> (2021).
48. Wobus, C., Helmsath, A., Whipple, K. & Hodges, K. Active out-of-sequence thrust faulting in the central Nepalese Himalaya. *Nature* **434**, 1008–1011 (2005).

**Publisher's note** Springer Nature remains neutral with regard to jurisdictional claims in published maps and institutional affiliations.

**Open Access** This article is licensed under a Creative Commons Attribution 4.0 International License, which permits use, sharing, adaptation, distribution and reproduction in any medium or format, as long as you give appropriate credit to the original author(s) and the source, provide a link to the Creative Commons license, and indicate if changes were made. The images or other third party material in this article are included in the article's Creative Commons license, unless indicated otherwise in a credit line to the material. If material is not included in the article's Creative Commons license and your intended use is not permitted by statutory regulation or exceeds the permitted use, you will need to obtain permission directly from the copyright holder. To view a copy of this license, visit <http://creativecommons.org/licenses/by/4.0/>.

© The Author(s) 2023



## Methods

### Extraction of topographic metrics

First, we isolated our analysis to the extent of the orogen<sup>49,50</sup>, including the tectono-stratigraphic units of the SHZ, the LHS, the Greater Himalayan sequence (GHS) and the THS and excluding both the western and eastern syntaxial regions. We then split the DEM into major river catchments using catchment outlines from the Hindu Kush Himalayan region<sup>47</sup> and limited our analysis to those draining to the southern edge of the orogen. We then analysed valley-floor width for every major river basin, using a method for reproducibly extracting valley-floor width from digital elevation models (DEMs)<sup>26</sup>. This method first identifies floodplains using a threshold of slope and elevation above the nearest channel<sup>25</sup>. These thresholds can either be set manually by the user or defined automatically; to ensure consistency across the orogen, we manually set a slope threshold of 0.15 and an elevation threshold of 100 m. The method then identifies the main flow direction of the channel and calculates valley-floor width orthogonal to this. The minimum possible width measurement is 60 m, which is set by the resolution of the DEM (2 DEM pixels).

Following extraction of width measurements for every channel, we removed any measurements that intersected each other (that is, at tributary junctions) as these measurements are unlikely to represent the true valley-floor width. We removed measurements from modern glaciers across the Himalayas using the glacier outline shapefiles from the Randolph Glacier Inventory<sup>51</sup>: we removed any measurements within the boundaries of each shapefile. Alongside modern glaciation, valleys that have been affected by glaciation through the Quaternary may have a topographic signature of glaciation rather than fluvial processes. We therefore performed a sensitivity analysis of our results to estimated glacial extents during the Last Glacial Maximum by estimating the minimum elevation of the LGM equilibrium line altitudes for glaciers across the orogen, using a regional compilation<sup>52</sup>. We found that removing the signature of Quaternary glaciations did not affect the results (Supplementary Figs. 1 and 2). After filtering, we gridded the valley-floor width data using a grid cell size of 10 km, taking the mean valley-floor width within each grid cell. We tested the sensitivity of the random forest regression to grid cell size (Supplementary Fig. 4) and found that the results were insensitive to gridding at cell sizes from 1 to 10 km.

We calculated the mean elevation of each 10 km valley-floor grid cell using the Copernicus 30 m DEM and determined the underlying tectono-stratigraphic unit using a geologic database<sup>50</sup>. We calculated normalized channel steepness ( $k_{sn}$  ( $m^{0.9}$ )) across each river basin using a segmentation approach<sup>53</sup> as implemented in LSDTopoTools<sup>54</sup>.  $k_{sn}$  is often used as a proxy for rock-uplift or erosion rates and has been shown to correlate with local relief and catchment-averaged erosion rate across the Himalaya (for example, refs. 55–59). We used a reference concavity value,  $\theta = 0.45$ , which has previously been estimated for the Himalayan region (for example, ref. 60). We gridded the  $k_{sn}$  data using the same approach as for valley-floor width (Fig. 2b).

To estimate water discharge,  $Q_w$ , we use a simple proxy based on weighting upstream drainage area ( $A$ ) by mean annual rainfall ( $P$ )<sup>30</sup>:

$$Q_w = PA, \quad (2)$$

We estimated  $P$  from 1981 to 2019 across the Himalaya using the Climate Hazards Group InfraRed Precipitation with Station (CHIRPS) dataset, which combines 0.05° resolution satellite imagery with ground-station data<sup>61</sup>. The advantage of using the CHIRPS dataset is that it has a near-global rainfall time series for more than 30 years, giving longer-term estimates of  $P$  that should be less sensitive to short-term temporal variations. We calculated  $P$  from this dataset using Google Earth Engine, then resampled  $P$  to a spatial resolution of 30 m to correspond to that of the topographic data. We test discharge rather than drainage area as the Himalaya have a strong orographic rainfall

gradient resulting in an order-of-magnitude variation in  $P$  across strike and an  $\approx$  sixfold increase in rainfall from west to east<sup>62,63</sup>. To test the ability of this simple model to reflect real variations in  $Q_w$ , we compared the model predictions to measured  $Q_w$  from gauging stations across major rivers in Nepal<sup>64,65</sup>. We found good agreement between modelled and measured  $Q_w$  across a range of discharges (Supplementary Fig. 5).

To investigate the potential impact of fracturing on bedrock erodibility, we also calculated the Euclidean distance of each grid cell from the nearest major tectono-stratigraphic boundary (either the Main Frontal Thrust (MFT), Main Boundary Thrust (MBT), Main Central Thrust (MCT) or South Tibetan Detachment (STD))<sup>50</sup>.

### Compilation of thermochronology data and calculation of exhumation rates

We updated an existing compilation of thermochronometric data from the Himalaya<sup>66</sup> to include more recent publications up to July 2022, including all data falling within the basins outlined in Fig. 2a. We include results from five thermochronometric systems in our analysis: apatite and zircon (U-Th)/He (AHe, ZHe) and fission track (AFT, ZFT) and white mica <sup>40</sup>Ar/<sup>39</sup>Ar (MAR). We removed any cooling ages  $\geq 50$  Ma, as these ages are pre-Himalayan<sup>49</sup> and are therefore unrepresentative of valley-forming processes, and samples from the SHZ, as these are generally incompletely reset since deposition<sup>67</sup>. In some cases, multiple thermochronometric cooling ages were available for a single location: we filtered the dataset to keep only the youngest age for these samples, as these are more likely to be representative of the erosion rate shaping the modern topography. We also filtered the dataset based on uncertainty by removing any samples where the  $1\sigma$  uncertainty in predicted exhumation rate was greater than the exhumation rate itself (Supplementary Fig. 6), and we removed any samples within the boundaries of modern glaciers<sup>51</sup>. The complete dataset and associated references can be found in ref. 24.

We use a 1D thermal model that assumes vertical exhumation and thermal steady state to estimate exhumation rates from the thermochronology data. The model (refer to ref. 24 for details) takes into account the advective perturbation of the geotherm by rapid exhumation<sup>68</sup> and the control of cooling rate on closure temperature of each thermochronometric system<sup>69</sup>. We use the sample elevation to estimate the surface temperature using a linear atmospheric lapse rate ( $5^\circ\text{C km}^{-1}$ ) and a constant sea-level temperature ( $25^\circ\text{C}$ ) and to estimate the vertical difference between the sample elevation and the average elevation smoothed within a radius that depends on the estimated closure depth of each thermochronometric system<sup>70</sup>. The latter is used to correct the estimated exhumation rate for relative sample elevation. For other model parameters, we assume the following: an initial linear geotherm of  $25^\circ\text{C km}^{-1}$ , a thermal diffusivity of  $30\text{ km}^2\text{ Myr}^{-1}$  and a model thickness of 30 km. We then mapped each exhumation rate sample to the corresponding valley-floor width cell in the gridded 10 km dataset and binned valley-floor width and  $k_{sn}$  by exhumation rate.

### Erodibility index

We calculated an erodibility index,  $K$ , for each of the main tectono-stratigraphic units across the Himalayan orogen using a compilation of catchment-averaged erosion rate data from cosmogenic radionuclides<sup>71</sup>, similar to the approach of ref. 72. The commonly used stream power incision model predicts a nonlinear relationship between channel slope and erosion rates:

$$E = KA^m S^n, \quad (3)$$

which we can rearrange to find an expression for channel slope,  $S$ :

$$S = \frac{E^{1/n}}{K} A^{-\theta}, \quad (4)$$

where  $\theta = m/n$ . We can simplify this equation to:

$$S = k_{sn}A^{-\theta}, \quad (5)$$

$$k_{sn} = E/K^{1/n}. \quad (6)$$

We estimate  $k_{sn}$  as described above and then assume that the CRN-derived erosion rates are representative of erosion across the entire basin, such that for each point on the network, we know  $k_{sn}$  and set  $E$  as the catchment-averaged erosion rate. We can then rearrange equation (6) to solve for erodibility at each point on the channel network,  $K_i$ :

$$K_i = \frac{E}{k_{sni}^n}. \quad (7)$$

Many studies have suggested through both numerical modelling and field studies that  $n$  is likely to be  $> 1$  (for example, refs. 72–74), with  $n \approx 2$  thought to be reasonable in most cases<sup>75</sup>. We therefore set  $n = 2$  in equation (7): a similar approach was also taken by ref. 76. As we set  $m/n = 0.45$  in our  $k_{sn}$  calculation, this results in  $m = 0.9$ . We then separate the calculated erodibilities based on tectono-stratigraphic unit and calculate the median  $K$  for each. The median values of  $K$  for each unit can be found in Supplementary Table 1.

A similar approach to calculating  $K$  can be taken, which also accounts for the impact of climate, by back-calculating  $K$  from the relationship between erosion rates and a channel steepness calculated by weighting drainage area by precipitation,  $k_{sn-q}$ <sup>77</sup>. We calculated  $k_{sn-q}$  and found that the relationship between  $W_v$  and  $k_{sn-q}$  was similar to that of  $k_{sn}$  (Supplementary Fig. 3). Furthermore, we found no relationship between  $P$  and  $W_v$ , suggested that weighting  $K$  by  $P$  is unlikely to change the relationship between  $K$  and  $W_v$ . Other approaches to estimating erodibility have derived an erodibility index that incorporates (1) a rock strength index ( $L_i$ ), related to its composition and (2) an age index based on the stratigraphic age of the unit<sup>78,79</sup>. We also tested this method of determining erodibility and found that it did not alter the relative importance in the random forest analysis (Supplementary Fig. 7).

### Random forest regression

Random forest (RF) regression is a form of supervised machine learning, which uses an ensemble of decision trees to predict a target variable (here  $W_v$ ) from a high-dimensional dataset (for example, ref. 80). It allows the calculation of variable importance (VI) for each variable used to predict the target variable. It requires no assumptions about the structure of the underlying data and therefore is useful in cases where the relationship between the target variable and the predictors is unknown a priori<sup>81</sup>. We performed RF regression on the 10 km gridded dataset to isolate the key signals of valley widening and reduce dataset noise. Supplementary Fig. 8 shows the spatial distribution of additional metrics used in the RF regression across the Himalayan orogen (elevation, water discharge, distance from nearest fault and tectono-stratigraphy). Before running the regression model, we split the gridded dataset into 80% training and 20% testing to allow for validation.

The number of decision trees ( $N_T$ ) used to build the regression model has shown to be important when using RF regression, particularly when investigating VI<sup>80</sup>. We therefore performed a sensitivity analysis on the regression varying the number of decision trees from 10 to 2,000 (Supplementary Fig. 9). This analysis showed that the root mean square error of the regression model became relatively insensitive when the number of decision trees is greater than 1,000, with root mean square error 167 m. We therefore ran all RF-regression runs with 1,000 decision trees to ensure greatest computational efficiency.

VI in random forest regression can be determined through two approaches: average impurity reduction and permutation reduction

(for example, refs. 82,83). Average impurity reduction<sup>80</sup> states that the importance (Imp) of any variable  $X_j$  in predicting the target variable,  $Y$ , can be calculated by summing the weighted impurity decreases  $p(t)\Delta i(s_t, t)$ , where  $t$  represents each node where  $X_j$  is used, and  $\varphi_m$  is tree  $m$  in the forest containing all trees  $m = 1, \dots, M$ :

$$\text{Imp}(X_j) = \frac{1}{M} \sum_{m=1}^M \sum_{t \in \varphi_m} \delta_{j,t} [p(t)\Delta i(s_t, t)], \quad (8)$$

where:

$$\delta_{j,t} = \begin{cases} 1 & \text{if } j_t = j \\ 0 & \text{otherwise,} \end{cases} \quad (9)$$

$p(t)$  is the proportion of samples reaching  $t$ , and  $j_t$  is the variable used to split node  $t$ <sup>83</sup>. This approach gives the most importance to the variable that most decreases the mean impurity across all trees in the forest. However, the impurity reduction approach has been shown to be biased towards predictors that have a large number of values<sup>84</sup>. Therefore, an alternative approach to estimating variable importance called permutation reduction has been suggested<sup>80</sup>, which estimates the change in the mean standard error of the regression model when permuting a variable. The reader is referred to ref. 80 and ref. 83 for a full derivation and discussion of permutation reduction VI. We performed a sensitivity analysis of the variable importances derived for the valley-floor width regression model to choice of VI metric across a range of different decision trees (Supplementary Fig. 10). We find that the VIs are insensitive to the number of decision trees used in the regression model and that the order of VI is identical with our chosen model run of 1,000 trees.

### Data availability

The thermochronometric dataset used in this paper is available through the Zenodo data repository (<https://doi.org/10.5281/zenodo.7053115>). The valley-floor width dataset is available through Durham University Collections (<https://doi.org/10.15128/r2z890rt27d>). Source data are provided with this paper.

### Code availability

The code for topographic analysis, including valley-floor width extraction, is available as part of the open-source LSDTopoTools software package<sup>54</sup>. The code to estimate exhumation rates from thermochronology data is available through the Zenodo data repository (<https://doi.org/10.5281/zenodo.7053218>).

### References

- Yin, A. & Harrison, T. M. Geologic evolution of the Himalayan-Tibetan orogen. *Annu. Rev. Earth Planet. Sci.* **28**, 211–280 (2003).
- Parsons, A. J., Hosseini, K., Palin, R. M. & Sigloch, K. Geological, geophysical and plate kinematic constraints for models of the India–Asia collision and the post-Triassic central Tethys oceans. *Earth Sci. Rev.* **208**, 103084 (2020).
- Randolph Glacier Inventory—a dataset of global glacier outlines: Central, SW, and SE Asia. RGI Consortium <https://doi.org/10.7265/4m1f-gd79> (2017).
- Owen, L. A. & Benn, D. I. Equilibrium-line altitudes of the Last Glacial Maximum for the Himalaya and Tibet: an assessment and evaluation of results. *Quat. Int.* **138–139**, 55–78 (2005).
- Mudd, S. M. et al. A statistical framework to quantify spatial variation in channel gradients using the integral method of channel profile analysis. *J. Geophys. Res. Earth Surface* **119**, 138–152 (2014).
- Mudd, S. et al. LSDTopoTools2 v0.5 <https://doi.org/10.5281/ZENODO.5788576> (2021).

55. Wobus, C. W., Whipple, K. X. & Hodges, K. V. Neotectonics of the central Nepalese Himalaya: constraints from geomorphology, detrital  $^{40}\text{Ar}/^{39}\text{Ar}$  thermochronology, and thermal modeling. *Tectonics* **25**, TC4011 (2006).
56. Kirby, E. & Whipple, K. X. Expression of active tectonics in erosional landscapes. *J. Struct. Geol.* **44**, 54–75 (2012).
57. Yang, R., Herman, F., Fellin, M. G. & Maden, C. Exhumation and topographic evolution of the Namche Barwa Syntaxis, eastern Himalaya. *Tectonophysics* **722**, 43–52 (2018).
58. Ojha, L., Ferrier, K. L. & Ojha, T. Millennial-scale denudation rates in the Himalaya of far Western Nepal. *Earth Surf. Dyn.* **7**, 969–987 (2019).
59. Wahyudi, D. R., Sinclair, H. D. & Mudd, S. M. Progressive evolution of thrust fold topography in the frontal Himalaya. *Geomorphology* **384**, 107717 (2021).
60. Gailleton, B. et al. Isolating lithologic versus tectonic signals of river profiles to test orogenic models for the Eastern and Southeastern Carpathians. *J. Geophys. Res. Earth Surf.* **126**, e2020JF005970 (2021).
61. Funk, C. et al. The climate hazards infrared precipitation with stations—a new environmental record for monitoring extremes. *Sci. Data* **2**, 150066 (2015).
62. Bookhagen, B. & Burbank, D. W. Topography, relief, and TRMM-derived rainfall variations along the Himalaya. *Geophys. Res. Lett.* **33**, L08405 (2006).
63. Bookhagen, B. & Burbank, D. W. Toward a complete Himalayan hydrological budget: spatiotemporal distribution of snowmelt and rainfall and their impact on river discharge. *J. Geophys. Res. Earth Surf.* **115**, 3019 (2010).
64. Andermann, C. et al. Connecting source and transport: suspended sediments in the Nepal Himalayas. *Earth Planet. Sci. Lett.* **351–352**, 158–170 (2012).
65. Andermann, C. et al. Impact of transient groundwater storage on the discharge of Himalayan rivers. *Nat. Geoscience* **5**, 127–132 (2012).
66. Thiede, R. C. & Ehlers, T. A. Large spatial and temporal variations in Himalayan denudation. *Earth Planet. Sci. Lett.* **371–372**, 278–293 (2013).
67. van der Beek, P. et al. Late Miocene—recent exhumation of the central Himalaya and recycling in the foreland basin assessed by apatite fission-track thermochronology of Siwalik sediments, Nepal. *Basin Res.* **18**, 413–434 (2006).
68. Mancktelow, N. S. & Grasemann, B. Time-dependent effects of heat advection and topography on cooling histories during erosion. *Tectonophysics* **270**, 167–195 (1997).
69. Dodson, M. H. Closure temperature in cooling geochronological and petrological systems. *Contribu. Mineral. Petrol.* **1973** 40:3 40, 259–274 (1973).
70. Willett, S. D. & Brandon, M. T. Some analytical methods for converting thermochronometric age to erosion rate. *Geochem. Geophys. Geosyst.* **14**, 209–222 (2013).
71. Codilean, A. T. et al. OCTOPUS: an open cosmogenic isotope and luminescence database. *Earth Syst. Sci. Data* **10**, 2123–2139 (2018).
72. Harel, M. A., Mudd, S. M. & Attal, M. Global analysis of the stream power law parameters based on worldwide  $^{10}\text{Be}$  denudation rates. *Geomorphology* **268**, 184–196 (2016).
73. Clubb, F. J., Mudd, S. M., Attal, M., Milodowski, D. T. & Grieve, S. W. The relationship between drainage density, erosion rate, and hilltop curvature: implications for sediment transport processes. *J. Geophys. Res. Earth Surf.* **121**, 1724–1745 (2016).
74. Perne, M., Covington, M. D., Thaler, E. A. & Myre, J. M. Steady state, erosional continuity, and the topography of landscapes developed in layered rocks. *Earth Surf. Dyn.* **5**, 85–100 (2017).
75. Lague, D. The stream power river incision model: evidence, theory and beyond. *Earth Surf. Process. Landforms* **39**, 38–61 (2014).
76. Zondervan, J. R., Stokes, M., Boulton, S. J., Telfer, M. W. & Mather, A. E. Rock strength and structural controls on fluvial erodibility: implications for drainage divide mobility in a collisional mountain belt. *Earth Planet. Sci. Lett.* **538**, 116221 (2020).
77. Leonard, J. S., Whipple, K. X. & Heimsath, A. M. Isolating climatic, tectonic, and lithologic controls on mountain landscape evolution. *Sci. Adv.* **9**, eadd8915 (2023).
78. Campforts, B. et al. Parameterization of river incision models requires accounting for environmental heterogeneity: insights from the tropical Andes. *Earth Surf. Dyn.* **8**, 447–470 (2020).
79. Wapenhans, I. et al. Scale-dependent contributors to river profile geometry. *J. Geophys. Res. Earth Surf.* **126**, e2020JF005879 (2021).
80. Breiman, L. Random forests. *Mach. Learn.* **45**, 5–32 (2001).
81. Grömping, U. Variable importance assessment in regression: linear regression versus random forest. *Am. Stat.* **63**, 308–319 (2009).
82. Louppe, G., Wehenkel, L., Sutter, A. & Geurts, P. Understanding variable importances in forests of randomized trees. *Adv. Neural Inf. Process. Syst.* **26**, 431–439 (2013).
83. Louppe, G. *Understanding random forests: from theory to practice*. Doctoral thesis, Université de Liège (2014).
84. White, A. P. & Liu, W. Z. Technical note: bias in information-based measures in decision tree induction. *Mach. Learn.* **15**, 321–329 (1994).

## Acknowledgements

We thank S. Tofelde, A. Densmore, R. Hodge, M. Allen and E. Dingle for useful discussions. LSDTopoTools software development was supported by a Durham Research Development Fund grant and Natural Environment Research Council (NERC) grants NE/P012922/1 (F.J.C.) and NE/S009000/1 (S.M.M.). For the purpose of open access, the authors have applied a Creative Commons Attribution (CC BY) licence to any author accepted paper version arising.

## Author contributions

F.J.C., S.M.M., H.D.S. and R.D. developed the study. F.J.C. and S.M.M. developed the topographic analysis code. F.J.C. performed the topographic analyses, the random forest regression and created the figures. T.F.S. and P.A.v.d.B. compiled the thermochronometry data and performed the exhumation rate calculations. F.J.C. wrote the paper with contributions from all authors.

## Competing interests

The authors declare no competing interests.

## Additional information

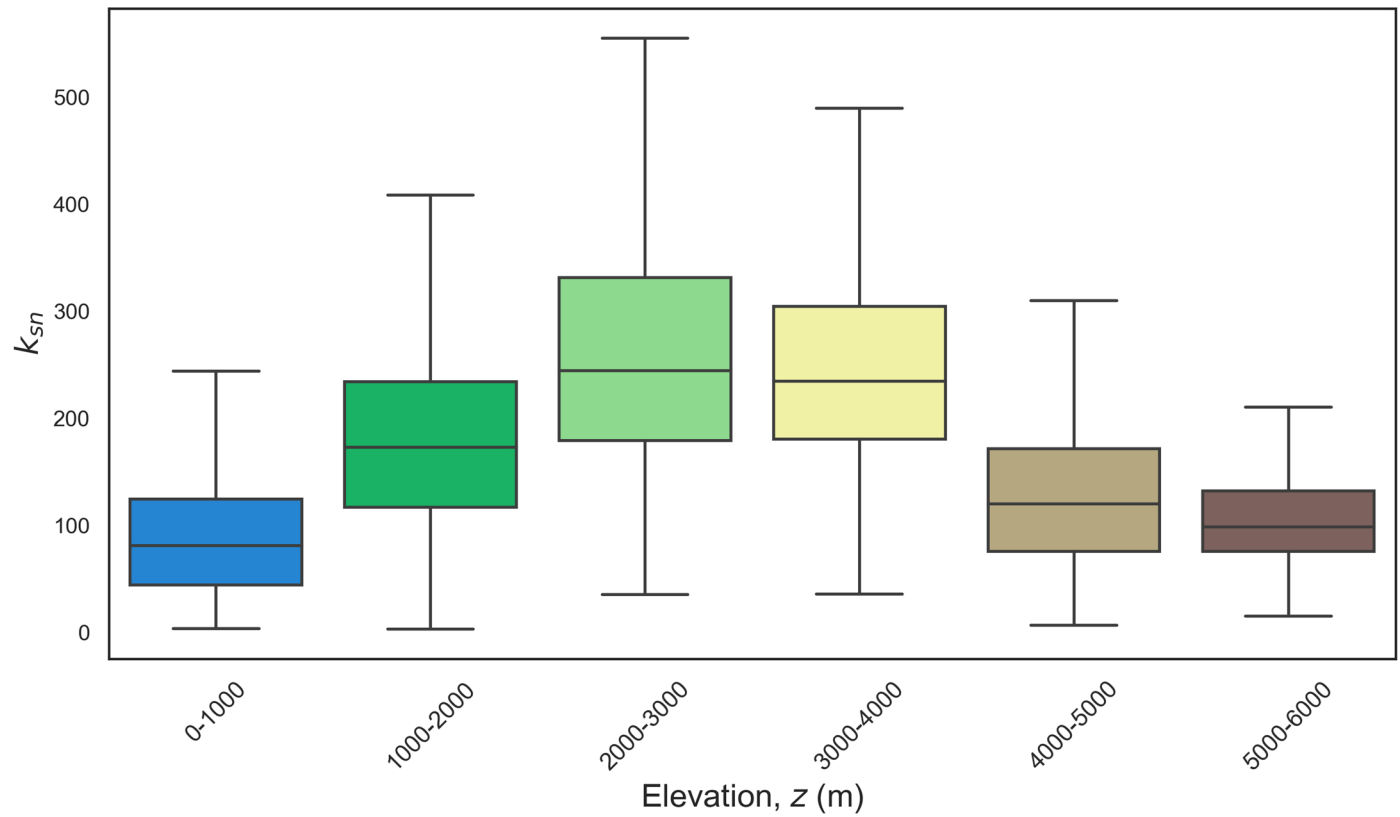
**Extended data** is available for this paper at <https://doi.org/10.1038/s41561-023-01238-8>.

**Supplementary information** The online version contains supplementary material available at <https://doi.org/10.1038/s41561-023-01238-8>.

**Correspondence and requests for materials** should be addressed to Fiona J. Clubb.

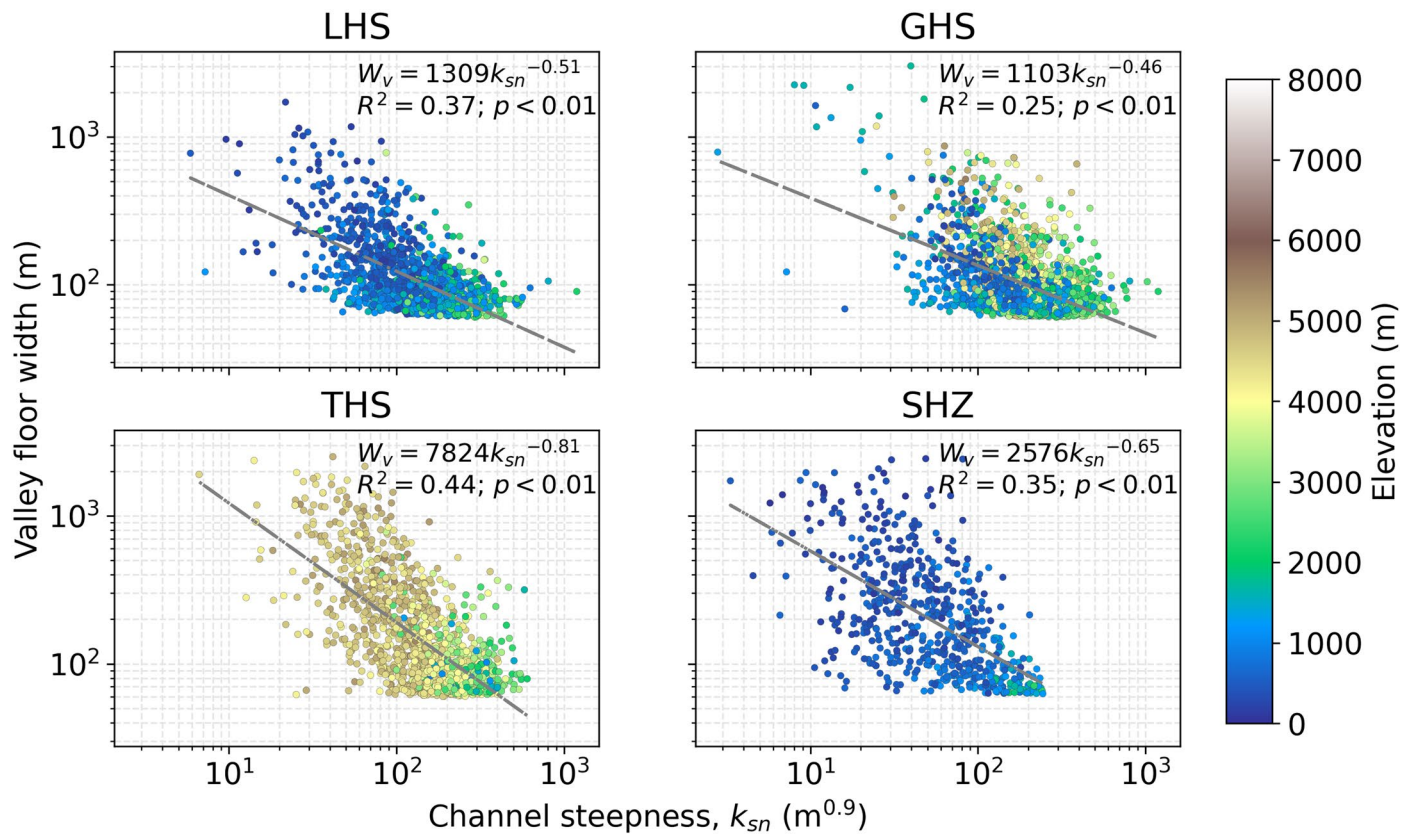
**Peer review information** *Nature Geoscience* thanks Adam Forte and the other, anonymous, reviewer(s) for their contribution to the peer review of this work. Primary Handling Editors: Louise Hawkins and Tom Richardson, in collaboration with the *Nature Geoscience* team.

**Reprints and permissions information** is available at [www.nature.com/reprints](http://www.nature.com/reprints).



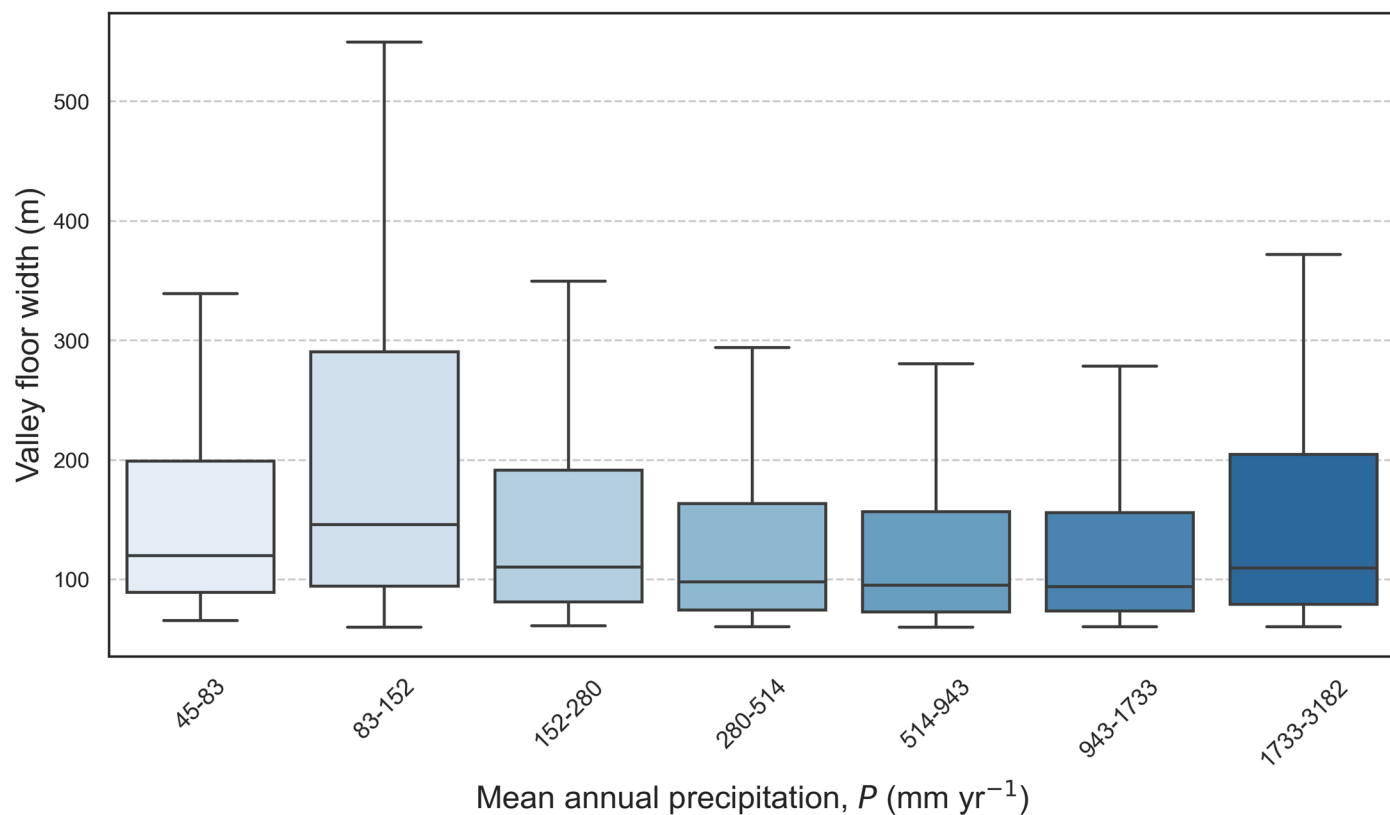
**Extended Data Fig. 1 | Boxplots showing the distribution of channel steepness with elevation.** Boxplots showing the relationship between  $k_{sn}$  and elevation across the Himalayan orogen ( $n=7,414$ ). The solid black line shows the

median of each distribution; the box represents the inter-quartile range; and the whiskers represent 1.5 times the inter-quartile range. **Minima and maxima have been omitted to ensure readability.**



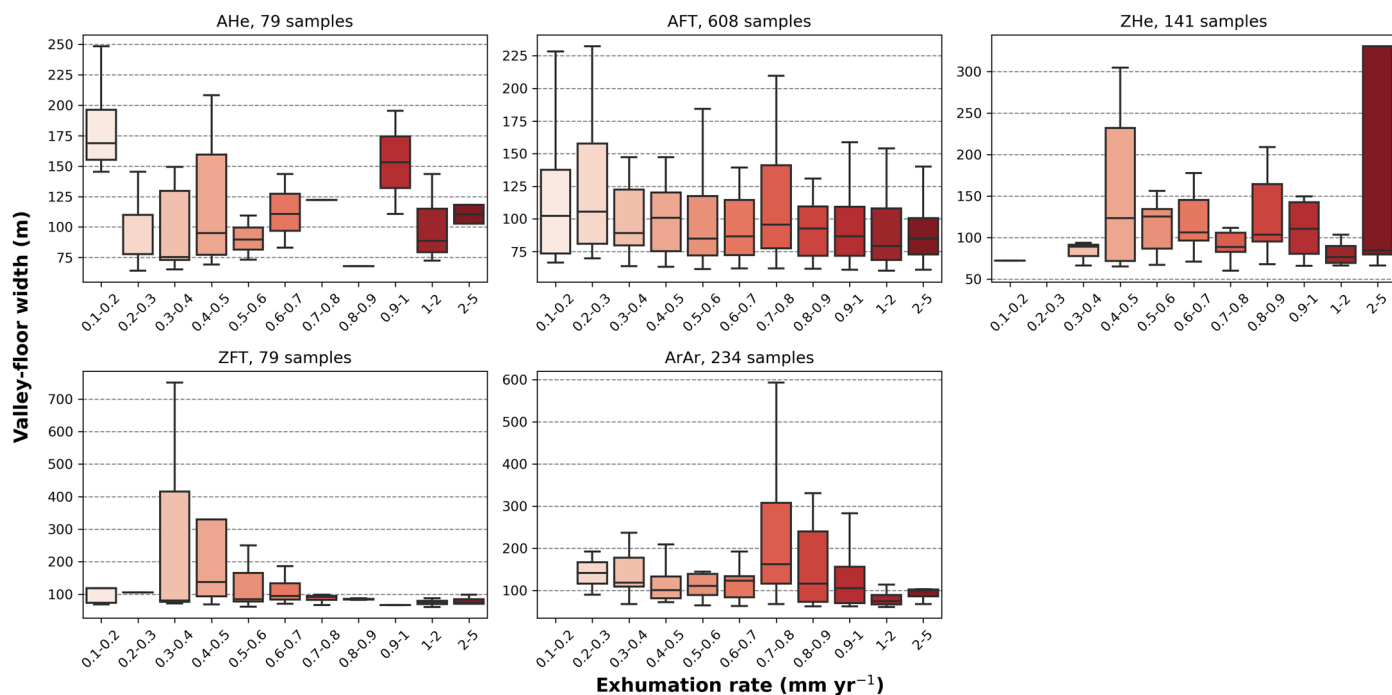
**Extended Data Fig. 2 | The relationship between valley-floor width and channel steepness, separated by tectono-stratigraphic unit.** The relationship between valley-floor width and  $k_{sn}$  separated by each stratigraphic unit, coloured by elevation. LHS = Lesser Himalayan Sequence, GHS = Greater Himalayan Sequence, THS = Tethyan Himalayan Sequence, SHZ = Sub-Himalayan

Zone. The dashed grey line shows a linear least-squares regression through the data in log-log space: the equation of the regression line,  $R^2$  and  $p$  value (two-sided) are noted. LHS:  $R^2 = 0.37$ ,  $p = 4.86 \times 10^{-145}$ ; GHS:  $R^2 = 0.25$ ,  $p = 8.76 \times 10^{-146}$ ; THS:  $R^2 = 0.44$ ,  $p = 1.63 \times 10^{-157}$ ; SHZ:  $R^2 = 0.35$ ,  $p = 6.58 \times 10^{-57}$ .



**Extended Data Fig. 3 | Boxplots showing the distribution of valley-floor width with mean annual precipitation.** Boxplots of valley-floor width against mean annual precipitation  $P$  from 1989-2019 extracted from the CHIRPS dataset<sup>64</sup>

( $n=7,414$ ). The solid black line shows the median of each distribution; the box represents the inter-quartile range; and the whiskers represent 1.5 times the inter-quartile range. **Minima and maxima have been omitted to ensure readability.**



**Extended Data Fig. 4 |** Boxplots showing the relationship between valley-floor width and thermochronometric-derived exhumation rate, separated by chronometric system. The number of samples in each plot is indicated (AHe, n=79; AFT, n=608; ZHe, n=141; ZFT, n=79; ArAr, n=234). The solid black

line shows the median of each distribution; the box represents the inter-quartile range; and the whiskers represent 1.5 times the inter-quartile range. Minima and maxima have been omitted to ensure readability.